A SiGe-Based 240-GHz FMCW Radar System for High-Resolution Measurements

Sven Thomas, *Member, IEEE*, Christian Bredendiek, *Member, IEEE*, and Nils Pohl *Senior Member, IEEE*

***Abstract*— In this paper, a fully integrated silicon-germanium (SiGe)-based compact high-resolution frequency-modulated continuous-wave (FMCW) radar sensor working in a frequency range from 198 to 250 GHz is presented. The wide modulation bandwidth of 52 GHz enables a range resolution better than 3 mm combined with a measurement accuracy in the micrometer regime. Together with a low power consumption of approximately 3.5 W, a high-focusing Teflon lens antenna, and a compact and robust housing, the presented radar system is capable of satisfying the needs of several novel measuring tasks. A compensated measurement accuracy of down to −0.5–0.4 μm is achieved, which is demonstrated by distance measurements using a laser interferometer reference. Additionally, a calibration technique is shown enabling multi-target measurements reaching to the theoretical limit of the range resolution. As the fundamental feedthrough of common frequency doubler architectures cause false targets in the range profile, a dielectric fundamental frequency filter is presented as well, filtering the fundamental feedthrough signal and thus removing the false target, improving the unambiguousness of the presented radar sensor.**

***Index Terms*— Distance measurement, high-speed integrated circuits, industrial electronics, microwave integrated circuits, millimeter wave radar, monolithic microwave integrated circuit (MMIC), radar, silicon germanium (SiGe), ultra-wideband radar.**

I. Introduction

NOWADAYS, radar-based measurement systems are experiencing an increasing importance for several industrial, security, and automotive applications. Especially in the field of industrial measurements under harsh conditions, e.g., in blast furnaces [1] or for tank level probing [2], [3], high-resolution imaging [4]–[6], material characterization [7], or security applications [8], [9], radar-based measurement systems are gaining relevance as an alternative to conventional measurement systems. To fulfill the increasing requirements for accuracy and resolution, higher frequencies enabling higher modulation bandwidths are essential. In the past, III–V technologies such as gallium arsenide (GaAs) were obligatory to reach operating frequencies above 200 GHz but were also suffering of high production costs, a low yield, and a small scale of integration, making these technologies inefficient and uneconomic for use in high volume, low cost measurement systems. Recent advances in silicon germanium (SiGe) technologies [10] are also capable of reaching frequencies of operation above 200 GHz while still combining the very large scale of integration and high yield inherent to silicon technologies. This enables a low-cost mass production.

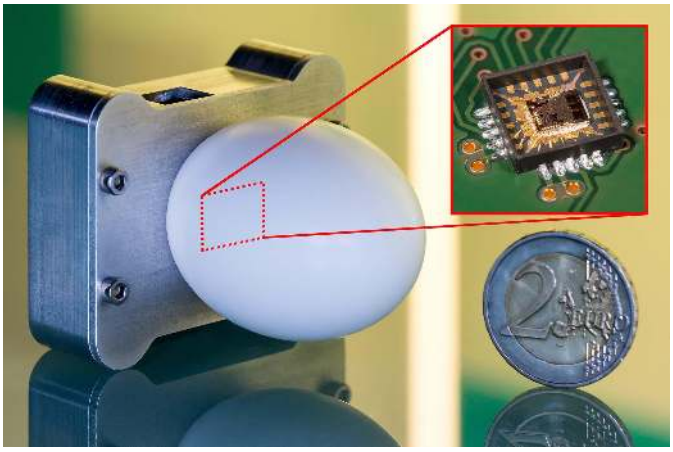

Fig. 1. Photograph of the compact FMCW sensor. Under the white PTFE lens antenna, the shown MMIC is located, packaged in an open cavity QFN.

Based on a fully integrated SiGe transceiver monolithic microwave integrated circuit (MMIC), an ultra compact, high-resolution, and high-accuracy radar sensor shown in Fig. 1 is presented. Compared to [11], the modulation bandwidth was improved by 12 GHz, resulting in an overall tuning range of 52 GHz. Additionally, a novel dielectric filter structure is presented, suppressing false targets caused by the fundamental feedthrough of the frequency doubler. As an IF-signal calibration based on the Hilbert transform is used, this method is analyzed in terms of the influence on the range resolution. The high bandwidth paired with a phase-locked loop (PLL) stabilized ramp generation, a dielectric fundamental frequency filter, and an IF signal calibration enable high-accuracy and high-resolution measurements catching up to conventional measurement systems for a wide range of industrial, automotive, or security applications. Besides the bistatic version of the MMIC, an additional monostatic version was developed and compared in terms of the antenna beamwidth and

Manuscript received December 31, 2018; revised March 29, 2019 and April 10, 2019; accepted April 19, 2019. Date of publication June 24, 2019; date of current version November 5, 2019. This work was co-funded by the German Research Foundation (DFG) through SFB/TRR 196 "MARIE," project C03. *(Corresponding author: Sven Thomas.)*

S. Thomas and C. Bredendiek are with the Department of Integrated Circuits and Sensor Systems, Fraunhofer Institute for High Frequency Physics and Radar Techniques, 53343 Wachtberg, Germany (e-mail: sven.thomas@fhr.fraunhofer.de; christian.bredendiek@fhr.fraunhofer.de).

N. Pohl is with the Institute for Integrated Systems, Ruhr-University Bochum, 44801 Bochum, Germany (e-mail: nils.pohl@rub.de).

Color versions of one or more of the figures in this article are available online at http://ieeexplore.ieee.org.

Digital Object Identifier 10.1109/TMTT.2019.2916851

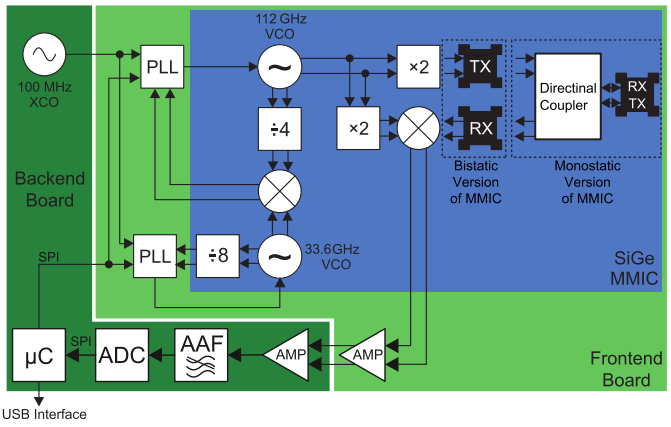

Fig. 2. Block diagram of the monostatic radar sensor, including back end, front end, and MMIC.

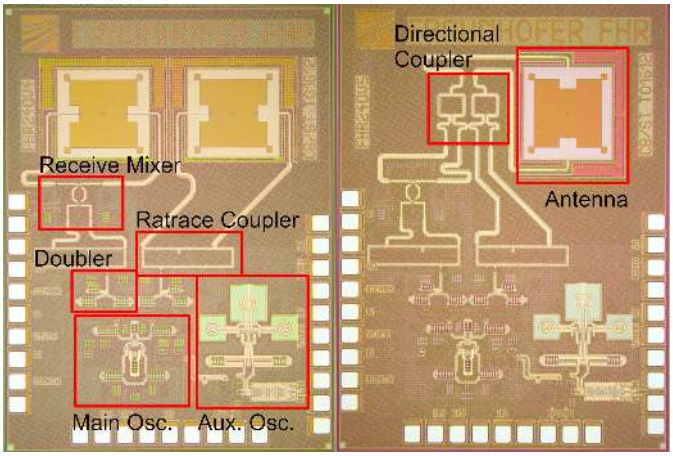

Fig. 3. Photograph of (left) bistatic and (right) monostatic SiGe transceiver MMIC.

dynamic range. The compact size of approximately 30 × 40 × 60 mm^3 allows an easy integration in existing or new applications even if only constricted room is available.

In the following, the system concept (Section II), the antenna setup (Section III), and characterization measurements, including calibration and filter techniques, (Section IV) are shown in detail. Additionally, a comparison of similar sensors is given in Section V, followed by a conclusion in Section VI.

II. System Concept

The realized ultra compact sensor is shown in Fig. 1 with the attached lens antenna and a detailed view of the MMIC. An overview of the complete system architecture is shown in Fig. 2. Basically, the sensor electronics consists of three components, a back-end board connected to a front-end board, which, in turn, carries the packaged MMIC as the third component. The IF signal coming from the MMIC is amplified by a first amplifier stage on the front-end board, which holds the analog components, including the MMIC, PLL chips, and loop filters. The back-end board carries the power supply, a reference crystal oscillator, and the digital part of the radar system, including a second amplifier stage and an anti-aliasing filter in front of the analog-to-digital converter, which samples the IF Signal coming from the front-end board. A micro-controller on the back-end board, which is also used for configuring the PLLs, transmits the sampled data via USB to a PC where the signal processing is done.

The core of the presented radar system is a fully integrated SiGe transceiver MMIC that combines all high-frequency components on a single die, which is mounted in an open cavity QFN package. As all high-frequency parts are on-chip, the front end can be realized using simple FR4 material, which allows an easy and cost-efficient fabrication of the sensor. The MMIC uses Infineons SiGe BiCMOS B11HFC technology presented in [12], which is intended for automotive purposes. It provides a bipolar process including a high-speed bipolar transistor reaching an $f_T = 250$ GHz and $f_{max} = 400$ GHz in combination with a 130-nm CMOS process. For realizing the presented MMIC, only the bipolar process was used. To generate the output signal, the main oscillator described in [13] is working at a center frequency of 112 GHz followed by two identical push–push frequency doublers, as described in [11], to generate the transmit signal with a center frequency of $f_c = 224$ GHz and feed the receive mixer, respectively. As the output frequency with up to $f_{out,max} = 250$ GHz is too high to be connected with bond wires, the MMIC uses fully integrated on-chip patch antennas as can be seen in the chip photograph in Fig. 3 for transmitting and receiving the signal directly on-chip. To focus the main beam, a dielectric lens antenna is placed above the mounted MMIC, as can be seen in Fig. 4. The sensors' frequency range covering $f_{out} =$ 198–250 GHz was selected to achieve a modulation bandwidth as large as possible while also covering the 244-GHz ISM band reaching from 244 to 246 GHz. This enables the radar sensor to operate in a high-resolution mode with a maximum modulation bandwidth of up to $B = 52$ GHz but also features a bandwidth limited ISM mode for license free operation for low-resolution applications.

Two versions of the transceiver MMIC were fabricated. One with two antennas in a bistatic configuration and another one with a single antenna in a monostatic configuration using a directional coupler consisting of two Wilkinson dividers, as shown in Fig. 5. The bistatic version is advantageous in terms of measurement dynamic because there is a much lower crosstalk from the transmit signal into the receive mixer but causes a displacement of each antenna out of the focal point of the lens. Vice versa, a monostatic setup causes a decreased measurement dynamic due to the directional coupler, which causes a higher crosstalk from TX to RX and which adds an additional 3-dB loss but ensures a common phase center in combination with the lens antenna. Section III will go into more detail about the antenna setup.

A. Receiver Performance

The receiver consists of the receive mixer followed by a preamplifier on the front-end board, a second amplifier on the back-end board, and an anti-aliasing filter in front of the ADC. For examining the receiver performance, an IF

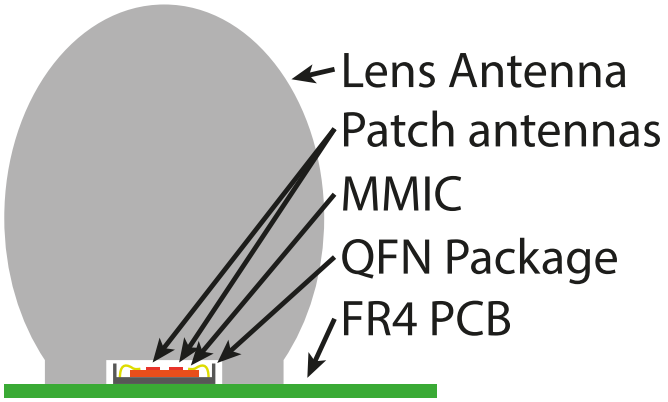

Fig. 4. Mechanical assembly of the PTFE lens antenna in front of the transceiver MMIC [11].

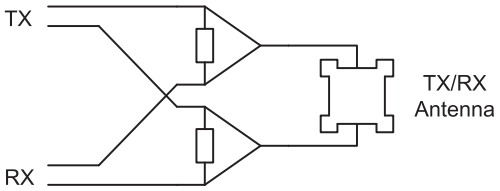

Fig. 5. Directional coupler for monostatic operation consisting of two Wilkinson dividers.

frequency of $f_{\mathrm{IF}} = 23$ kHz was used, which corresponds to a distance of $d = 1$ m using the standard ramp parameters with $B = 52$ GHz modulation bandwidth and $T_{\mathrm{ramp}} = 15$ ms sweep time. The anti-aliasing filter is an active ninth-order low-pass filter with a corner frequency of f_c, AAF $= 360$ kHz, which corresponds to a maximum detection distance of $d_{\mathrm{max}} \approx 15.6$ m with standard ramp parameters mentioned above. The receive mixer is using a fully differential gilbert cell architecture and offers a simulated voltage gain of G_v, mixer $=$ 16.75 dB, which corresponds to a simulated power gain of approximately G_p, mixer ≈ 0 dB due to the different impedance levels (100 Ω at RF-input and high ohmic at IF-output). The noise figure of the receive mixer is simulated to be $\mathrm{NF}_{\mathrm{mixer}} = 13.89$ dB. The baseband IF path including preamplifier, amplifier and anti-aliasing filter features a simulated voltage gain of G_v, IF, baseband $= 25.38$ dB and a noise figure of $\mathrm{NF}_{\mathrm{IF,baseband}} = 17.23$ dB. In monostatic operation, the losses of the directional coupler, which is based on two Wilkinson dividers, have to be considered. The losses caused by the coupler were simulated to be $L_{\mathrm{coupler}} =$ 3.74 dB using CST microwave studio. As the coupler is a passive structure, the noise figure is equal to the loss $\mathrm{NF}_{\mathrm{coupler}} = L_{\mathrm{coupler}} = 3.74$ dB.

According to the Friis formula, the overall receiver noise figure can be determined to be $\mathrm{NF}_{\mathrm{receiver,bistatic}} = 18.83$ dB for bistatic configuration and $\mathrm{NF}_{\mathrm{receiver,monostatic}} = 22.57$ dB for monostatic operation, respectively. The overall receiver voltage gain is calculated to $G_{\mathrm{v,receiver,bistatic}} = 42.13$ dB for bistatic operation and $G_{\mathrm{v,receiver,monostatic}} = 38.39$ dB for monostatic operation, respectively.

For examining the linearity of the receive mixer, the 1-dB compression point and the input-referred third-order intercept point were simulated to be CP1 $= -3.86$ dBm and $IIP3 = 5.79$ dBm. Assuming a receive power 10 dB below CP1 for linear operation, the maximum receive power for linear operation is $P_{r,\mathrm{max,lin}} = -13.86$ dBm. The antenna gain of the lens antenna is simulated to be $G_{\mathrm{lens}} = 35$ dBi. By calculating the receive power for a given distance, the minimal measurement distance beyond a linear operation can be determined. For the bistatic version, this distance is given by $d_{\mathrm{min,lin,bistatic}} \approx 1$ m and for the monostatic version $d_{\mathrm{min,lin,monostatic}} \approx 0.43$ m due to the additional losses of the directional coupler. This means, that for measurement distances below $d_{\mathrm{min,lin,bistatic}}$ or $d_{\mathrm{min,lin,monostatic}}$, there might be nonlinear effects for electrically large and strong targets. But for the intended use-cases of the radar system such as single-target distance measurements, the effects caused by the receivers' nonlinearities are negligible. If there are applications which require a high linearity even for short distances such as imaging or layer thickness measurements, another lens antenna with less gain can be used, reducing $d_{\mathrm{min,lin,bistatic}}$ or $d_{\mathrm{min,lin,monostatic}}$ when needed.

B. Tuning Range

As shown in Fig. 2, the main oscillator is stabilized by using an offset PLL concept. An Hittite HMC704 integer-N PLL is used to stabilize a fixed auxiliary oscillator with $f_{\mathrm{aux}} = 33.6$ GHz. This auxiliary signal is used for mixing the divide-by-4 output of the main oscillator in reverse frequency position down to the input signal of the programmable frequency divider of the main sweeper PLL realized by a Hittite HMC701 chip. Due to this mixing process, the variation of the main PLLs' closed-loop gain over frequency is compensated as described in [14]. This allows a wide tuning range of $f_{\mathrm{fund}} = 99$–125 GHz, leading to an output frequency of $f_{\mathrm{out}} =$ 198–250 GHz behind the frequency doubler. This corresponds to a continuous frequency tuning range of $B = 52$ GHz. Fig. 6 shows the measured tuning curve of the transceiver chip. The overall tuning range covers 197.9 to 251.7 GHz resulting in 53.8 GHz, which is limited to the mentioned range of 198–250 GHz by the sweeper to ensure a reliable and robust PLL locking and sweep generation even under temperature and process variations.

C. Phase Noise

As the PLL stabilization is using the down-converted signal outputs of the transceiver MMIC, the phase noise of the high-frequency transmit signal has to be measured directly in front of the antenna. This was realized by using a Rohde & Schwarz FSWP50 signal analyzer equipped with a WR-3 down-conversion mixer mounted to a standard gain horn antenna to receive the radiated transmit signal. Fig. 7 shows the PLL-stabilized phase noise, which was measured at an oscillating frequency of $f_{\mathrm{out}} = 220$ GHz. Read from Fig. 7, the loop bandwidth of the synthesizer PLL is $f_{\mathrm{loop}} \approx 3$ MHz. For comparison of the in-loop phase noise, an offset frequency of $f_{\mathrm{offset,ref}} = 10$ kHz was chosen. The PLLs' in-loop phase

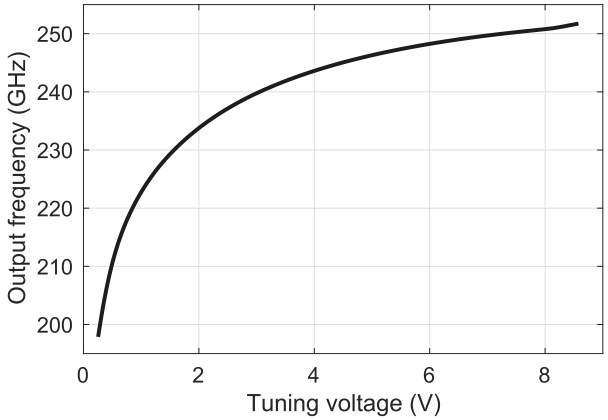

Fig. 6. Measured tuning range of the output signal of the transceiver MMIC.

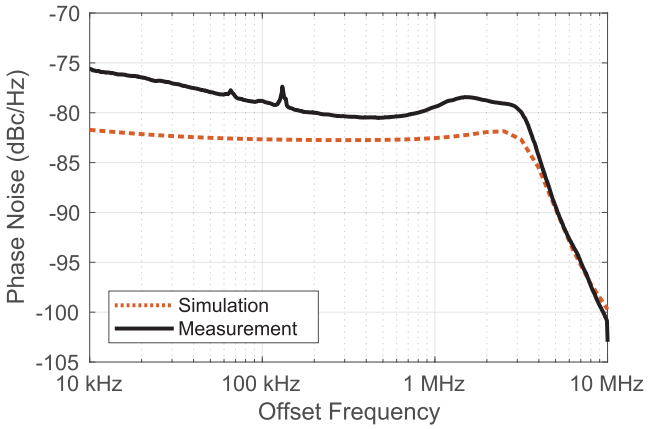

Fig. 7. Measured and simulated phase noise of the transceivers' output signal at 220 GHz.

noise is measured to be $\mathrm{PN}_{\text{in-loop}} = -75.6$ dBc/Hz at 10-kHz offset, which corresponds to a phase noise of $\mathrm{PN}_{\text{in-loop,fund}} = -81.6$ dBc/Hzof the main oscillators' fundamental signal before frequency doubling.

The minimum phase noise inside the loop bandwidth is measured at an offset frequency of $f_{\text{offset}} = 480$ kHz with $\mathrm{PN}_{\text{in-loop,min}} = -80.5$ dBc/Hz, which corresponds to a phase noise of $\mathrm{PN}_{\text{in-loop,min,fund}} = -86.5$ dBc/Hz of the main oscillator's fundamental signal. The maximum deviation between simulation and measurement can be observed for low offset frequencies and is given by $\Delta_{\text{meas,sim}} \approx 6$ dB which represents good results. As the presented synthesizer was optimized for a large bandwidth, it features a reliable locking over the complete tuning range of $B = 53.8$ GHz from 197.9 to 251.7 GHz using an offset PLL architecture described in [14]. Despite this offset PLL architecture minimizes the variation of the closed-loop gain over frequency, a certain variation of the closed-loop gain and, therefore, a variation of the phase noise has to be expected. Unfortunately, the phase noise measurement toward the lower and upper edges of the frequency range was not possible due to the combination of the decreasing output power discussed in Section III-B, the losses of the measurement setup, and the measurement dynamic range of the signal analyzer.

III. Antenna Setup

At high frequencies up to $f_{\text{out,max}} = 250$ GHz, even short bond wires lead to a parasitic series inductance which in combination with the pad capacitance toward ground causes too much loss making a bond interface unfeasible. For this reason, on-chip patch antennas are used for transmitting and receiving the signal directly on-chip. As these on-chip patch antennas are quite small with a dimension of $l_{\text{patch}} \approx 310\ \mu$m, the main beam of this antenna type is quite large with $\phi \approx 90°$, which makes it unfeasible for the intended use where a narrow pencil beam for a well-defined measurement spot is desired. To focus the on-chip antenna beam, an additional PTFE lens is placed above the MMIC. The mechanical assembly of the FR4 PCB, the QFN package with the MMIC, and the lens antenna is given schematically in Fig. 4. The lens further described in [15] is a rotation-symmetric ellipsoid milled out of a solid PTFE rod. The feed antenna is positioned in one of the ellipsoidal focal points.

A. Directivity

As mentioned earlier, a monostatic and a bistatic version of the MMIC are available. While the first version has individual antennas for TX and RX [see Fig. 3 (left)], the second version uses a directional coupler made of two Wilkinson dividers to combine the TX and RX channels in one single patch antenna [see Fig. 3 (right)]. According to the radar equation given by

$$P_{\text{RX}} = P_{\text{TX}} \frac{\eta^2\ D_{\text{RX}} D_{\text{TX}} \lambda^2 \sigma}{(4\pi)^3 r^4} \tag{1}$$

where P_{RX} and P_{TX} are the receive and transmit power, η is the efficiency of a single antenna, σ is the radar cross section, λ is the wavelength, r is the distance to the radar target, and D_{RX} and D_{TX} are the receive antenna directivity and the transmit antenna directivity, respectively. and the product of D_{RX} and D_{TX} can be interpreted as a combined TX/RX antenna pattern providing the effective beamwidth.

For the monostatic version, D_{RX} is equal to D_{TX}, so the resulting combined beamwidth can be determined by simulating the directivity of a single antenna under the PTFE lens and squaring the result. The resulting, normalized antenna pattern is shown in Fig. 8. The slightly tilted beam direction to the left is caused by the monostatic antenna position on the MMIC [Fig. 3 (right)], which is not centered on the MMIC; therefore, the patch is not directly located in the focal point of the lens. Additionally, a measurement was taken by fixing the radar sensor on a rotational stage with a corner reflector mounted on a fixed baseplate in a fixed distance. By turning the radar passing the corner reflector and measuring the signal amplitude at the corner distance, the combined, normalized pattern was recorded, which is also shown in Fig. 8. The simulation and measurement fit very well, which validates the monostatic beamwidth of $\phi_{\text{MS,3 dB}} = 1.415°$.

The bistatic version combined with the dielectric PTFE lens causes a displacement of each antenna out of the focal point of the lens antenna, leading to tilted TX and RX beams in opposite directions. Simulations made with CST Microwave Studio 2018 has shown that a bistatic antenna distance of

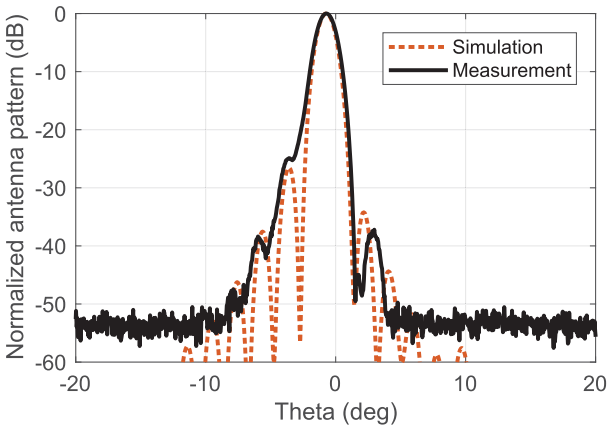

Fig. 8. Simulation and measurement of the normalized, combined TX/RX antenna pattern for the monostatic version of the MMIC at 240 GHz.

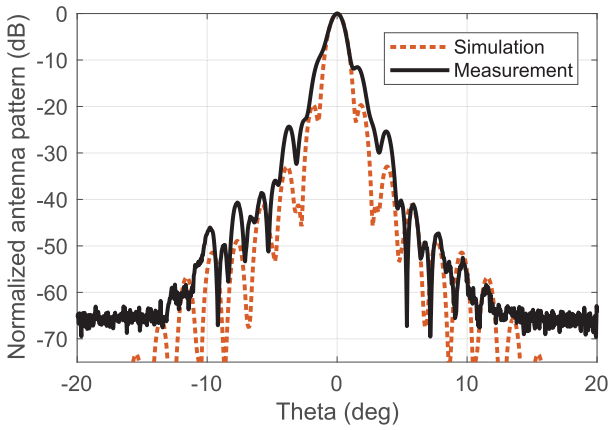

Fig. 9. Simulation and measurement of the normalized, combined TX/RX antenna pattern for the bistatic version of the MMIC at 240 GHz.

$d_{\text{antenna}} = 580\ \mu$m corresponding to a displacement of 290 μm for each antenna leads to a tilted beam direction of $\delta_{\text{tilt}} = 0.73°$ or $\delta_{\text{tilt,BS}} = 1.46°$ between the TX and RX beams. To determine the resulting TX/RX beamwidth in a bistatic configuration, the tilted directivity of one single antenna was simulated and multiplied with the flipped single antenna beam, which can be seen in Fig. 9. Additionally, once again a measurement for verification was taken. The main lobe shows a good agreement between simulation and measurement and shows a combined main lobe width of $\phi_{\text{BS,3 dB}} = 1.153°$, which is narrower than the monostatic configuration despite the squint-eyed TX and RX beams in the bistatic scenario. Further simulations have shown that this effect is caused by the interference of the side lobes and zeros of TX and RX antenna patterns. The deviation of the sidelobes' amplitude between simulation and measurement can be explained by mechanical inaccuracies of attaching the lens in front of the MMIC.

Additionally, when comparing the measurements in Figs. 8 and 9, an increased noise floor for the monostatic version can be observed. This is caused by the additional directional coupler, mandatory for monostatic operation. The coupler causes a simulated loss of $L_{\text{coupler}} = 3.74$ dB from each signal port to the antenna port. As the signal has to pass the coupler in both directions, TX and RX, the losses sum up to $L_{\text{coupler,TXRX}} = 7.48$ dB, leading to a decreased SNR visible in Figs. 8 and 9.

B. EIRP

To measure the output power of the radar system, the EIRP without the PTFE lens antenna was measured by an R&S FSEK40 spectrum analyzer equipped with an external RPG SAM-325 WR3.4 waveguide mixer. For covering the frequencies beyond the specified WR3.4 band, the RF over range feature was used and validated with an RPG FS-Z220 WR5.1 waveguide mixer. As the wavelength of the lowest frequency $f_{\text{min}} \approx 198$ GHz is approximately $\lambda_{\text{max}} \approx 1.5$ mm, the open-ended waveguide of the mixer acting as a receive antenna was placed above the TX on-chip antenna in a distance of $d_{\text{Ant}} = 10$ mm to ensure far-field conditions for both antennas. For aligning MMIC and mixer, an *xy* positioning table was used maximizing the detected input power of the spectrum analyzer. The EIRP was calculated from the measured receive power of the mixer by

$$\text{EIRP} = \frac{(P_{\text{meas}} + L_{\text{WG}})(4\pi d_{\text{Ant}})^2}{G_{\text{WG}}\lambda^2} \tag{2}$$

where P_{meas} is the measured power, L_{WG} is the calculated loss caused by the length of the used waveguide, and G_{WG} is the gain of the open-ended waveguide of the mixer used as the receive antenna. The conversion loss of the mixer was already considered in the spectrum analyzer measurement. The frequency-dependent open waveguide gain G_{WG} was calculated using [16], leading to a measured EIRP shown in Fig. 10 with a maximum EIRP of $\text{EIRP}_{\text{max}} = 0.58$ dBm. To determine the doubler output power, the gain of the on-chip antenna was simulated using CST Microwave Studio, leading to a maximum gain of $G_{\text{on-chip,max}} = -0.2$ dB, which decreases to the edges of the frequency band down to $G_{\text{on-chip,min}} = -6.36$ dB. The low gain can be explained with the low distance of the on-chip patch antenna in the upper metal layer to the ground plane in the lower metal layer in the MMICs' metal stack. As this distance is given by the used technology and is much lower than the desired $\lambda/2$, the efficiency decreases due to increased capacitive losses. Using the simulated gain values of the on-chip patch, the output power of the frequency doubler was back-calculated and is also shown in Fig. 10, reaching up to $P_{\text{out,max}} = 1.8$ dBm. Toward lower frequencies, a drop in output power can be observed, which is also responsible for the amplitude modulation of the IF signal further discussed in Section IV-B. This effect is mainly caused by the input impedance of the antenna. The output network of the frequency doubler was optimized to the input impedance of the patch antenna at center frequency. As the on-chip patch antenna is a resonant structure, the input impedance suffers a large variation in wideband operation leading to a mismatch toward the edges of the frequency band, affecting the output power of the frequency doubler.

IV. Distance Measurements

As the accurate measurement of the distance in industrial applications is the core function of the presented radar sensor,

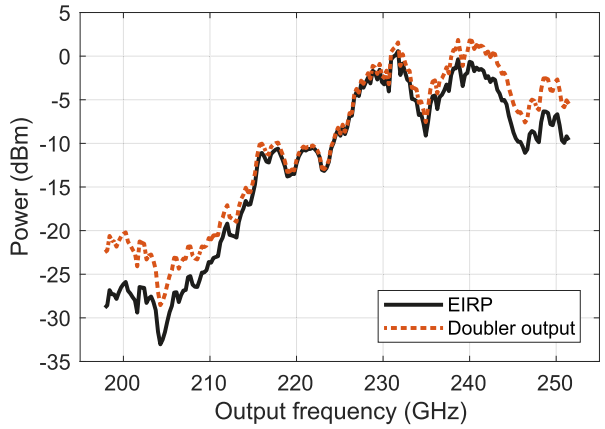

Fig. 10. Measured EIRP of the on-chip patch antenna without PTFE lens attached and back-calculated output power of the frequency doubler.

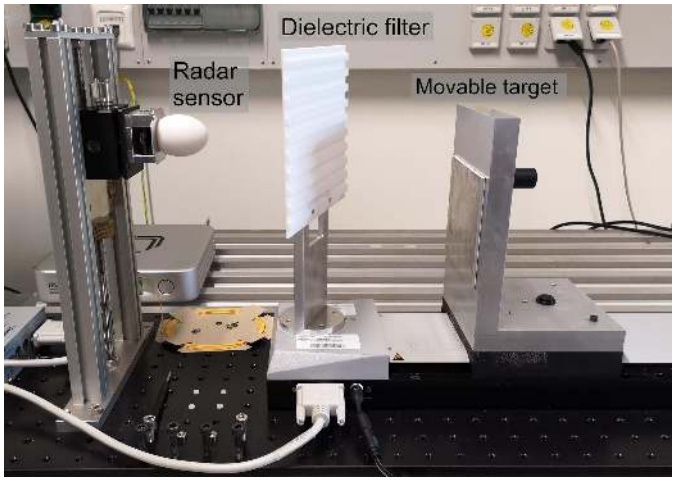

Fig. 11. Photograph of the distance measurement setup with radar sensor on the left, a dielectric filter in the middle, and movable target on the right.

the focus of the measurements was laid on short distances in particular. The bistatic version of the presented sensor showed the best performance in terms of measurement dynamic, which can be observed by the noise floor level in Figs. 8 and 9. Thus, the following measurements were done with the bistatic version. For the signal processing calculating the measured distance, an FFT-based amplitude evaluation combined with a barycenter calculation of the spectral peak was used. As frequency chirp, a down ramp ranging from 250–198 GHz with a ramp time of 15 ms was used.

In Fig. 11, a photograph of the distance measurement setup is shown. On the left-hand side, the radar sensor is mounted pointing to a movable target, which can be seen on the right-hand side. In the middle, directly in front of the radar sensor, a dielectric filter is positioned, which is described in Section IV-A.

A. Dielectric Fundamental Frequency Filter

As shown in Fig. 2, the output signal is generated by frequency-doubling the output signal of a fundamental oscillator. Common frequency doubler architectures suffer from a limited isolation of the fundamental frequency input to their output signal. This unwanted radiation at the fundamental frequency causes false targets in radar operations at the exact half of the targets' distance. An obvious way to reduce the false targets' amplitude is to increase the isolation of the fundamental frequency. In [17], an earlier version of the presented radar sensor is shown using a Gilbert cell doubler achieving a false target suppression of 22 dB below the main target. The current, presented version of the MMIC uses a push–push doubler concept described in [11], which offers an increased fundamental frequency isolation improving the false target suppression by 26 dB to a value of 48 dB below the main target. To further improve the false target suppression, the unwanted fundamental frequency has to be filtered or blocked to prevent an unwanted radiation.

For this purpose, the dielectric fundamental frequency filter shown in Fig. 11 was built. This filter made from PTFE has a slotted profile inserted perpendicular to the radars' main beam, as shown in Fig. 12. The equally spaced slots and bars milled in the PTFE plate cause the radar beam to see two different transmission lengths through the PTFE leading to a phase shift between the part of the beam passing the slots and the bars, respectively. The depth of the slots has to be selected to cause a phase shift of $\Delta\phi_{\text{fund}} = 180°$ for the fundamental frequency and $\Delta\phi_{\text{doub}} = 360°$ for the wanted doubled signal. In this case, the fundamental signal cancels out in the far field of the filter while the wanted, doubled signal transmits through the filter. As the phase shift between the propagation through a slot and the propagation through a bar is given by

$$\Delta\phi = 2\pi \frac{d_{\text{slot}} f}{c_0} \left(\sqrt{\epsilon_{\text{r,PTFE}}} - \sqrt{\epsilon_{\text{r,Air}}}\right) \tag{3}$$

the depth of the milled slots has to be

$$d_{\text{slot}} = \frac{c_0}{2 \cdot 112\ \text{GHz}\left(\sqrt{2.1} - 1\right)} = 2.9798\ \text{mm} \tag{4}$$

to achieve the desired canceling of the fundamental signal and transmission of the doubled signal, as shown in Fig. 12.

The result can be seen in Fig. 13, where the measured IF spectra of a single-target scenario are shown, measured with and without the dielectric filter. In both measurements, the multiple reflections from inside the lens antenna can be seen for close distances, decreasing in amplitude for increasing distances. As the received signal also causes multiple reflections inside the lens antenna, these antenna peaks also occur behind the main target. Focusing on the differences between the two measurements, the first measurement recorded without a dielectric filter clearly shows the false target. It is located at the exact half of the main targets distance, 48 dB below the main targets' amplitude. In the second measurement recorded with the dielectric filter, the false target disappears completely by successfully filtering the fundamental frequency signal out of the transmit signal. To suppress the echo of the filter surface, it is tilted in azimuth to deflect the surface reflection away from the receiver as can be seen in Fig. 11. For later realizations for use in industrial scenarios, this filter can easily be integrated in a housing of the sensor, allowing a sealed and robust sensor head.

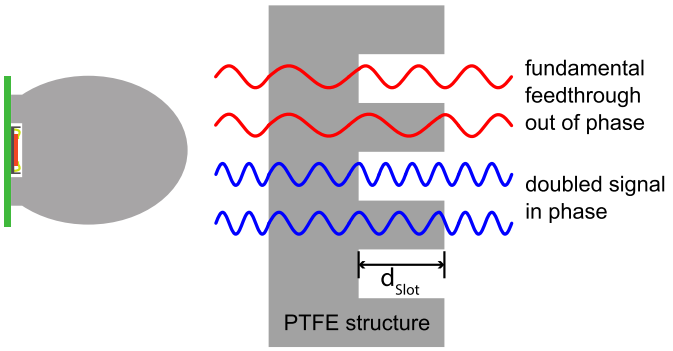

Fig. 12. Sketch of the dielectric fundamental frequency filter to filter out the unwanted fundamental feedthrough.

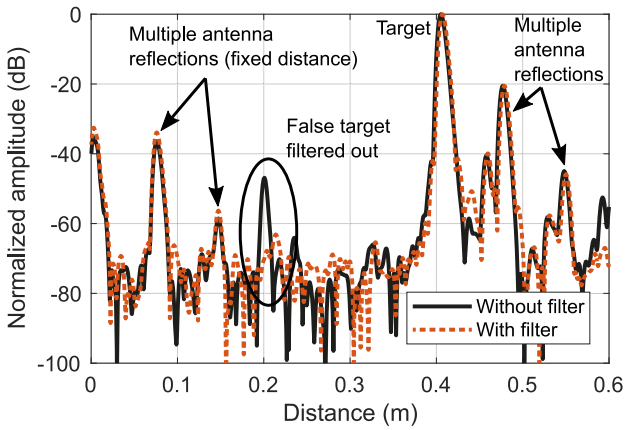

Fig. 13. Measured spectrum of a single target with and without fundamental frequency filter.

B. Range Resolution

Especially in multi-target environments or for imaging applications, a high range resolution is essential. Normally, the minimum range resolution with a rectangular window is given by

$$\Delta r = \frac{c_0}{2B} \tag{5}$$

where B is the modulation bandwidth of the FMCW sweep. For the used bandwidth of 52 GHz, this would be a possible range resolution of $\Delta r = 2.88$ mm. Preventing to reach this range resolution out of the box is the challenging disadvantage of the on-chip patch antennas to operate resonant and, therefore, narrowband but being used in a wideband system. Due to the increasing mismatch toward the edges of the frequency range in combination with the drop in output power mentioned in Section III, the radiated and received power decreases toward the edges. This effect leads to an amplitude modulation of the received IF-signal. The resulting modulation on the sampled IF-Signal is shown in Fig. 14.

This amplitude modulation of the IF signal acts as a window function causing a widening of the target peak in the IF spectrum, which, in turn, is decreasing the possible range resolution. As the modulating shape only depends on the system itself without any variance, the amplitude can be calibrated. In [7], a calibration procedure based on a common

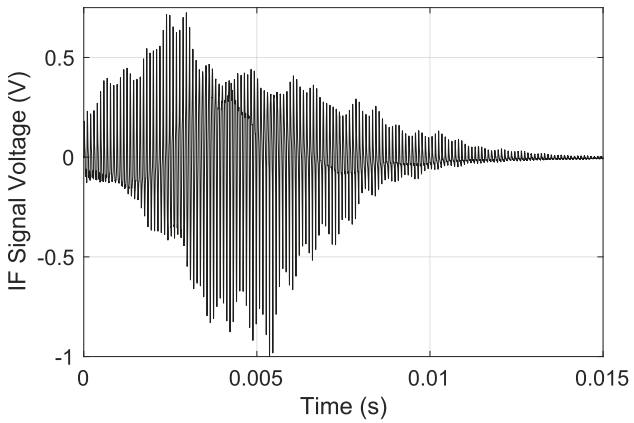

Fig. 14. Recorded IF-signal for a single target with visible decreasing amplitude toward the edges.

LRM calibration is presented, which is used to calibrate a radar sensor for material characterization. As this calibration procedure aims for compensating a complex error model describing the whole sensor, it requires the measurement of three known calibration standards (SHORT, LINE, and MATCH). In the presented case for increasing the range resolution by compensating the modulation of the IF signal, a simpler calibration is sufficient. As only the amplitude response has to be determined, the calibration effort can be reduced to one reference measurement of a SHORT standard, represented by a single reflector in front of the radar, which can even be measured in-line. Based on this calibration method, a single-target IF signal can be interpreted as

$$s_{\text{ref}}(t) = m(t) \cdot \cos(\omega_{\text{ref}} t + \phi(t)) \tag{6}$$

with $m(t)$ as the unwanted modulating function caused by the antenna mismatch and $\phi(t)$ as an error phase, both solely depending on the sensor itself. The corresponding ideal, theoretical, complex IF signal is given by

$$s_{\text{ideal}}(t) = e^{j\omega_{\text{ref}} t}. \tag{7}$$

To calculate the calibration factor $c(t)$, the complex reference IF signal is calculated by the Hilbert transformation

$$c(t) = \frac{s_{\text{ideal}}(t)}{\mathcal{H}\{s_{\text{ref}}(t)\}} = \frac{1}{m(t)} \cdot e^{-j\phi(t)}. \tag{8}$$

By applying the calibration factor on an arbitrary IF signal recorded with the same sensor, the amplitude modulation can be removed from the IF signal, enabling the use of the full bandwidth

$$s_{\text{meas,cal}}(t) = \mathcal{H}\{s_{\text{meas}}(t)\} \cdot c(t) \tag{9}$$

$$= \cancel{m(t)} e^{j\omega_{\text{ref}} t + \cancel{\phi(t)}} \cdot \frac{1}{\cancel{m(t)}} \cancel{e^{-j\phi(t)}}. \tag{10}$$

In Fig. 15, a comparison of the IF spectrum of an uncalibrated and calibrated IF signal is shown. The IF signal was recorded with a metal plate as main target with a plate of 3-mm thickness attached with 200-μm-thick adhesive tape, representing a dual target scenario with two targets spaced 3.2 mm from each other. As reference measurement for calculating the

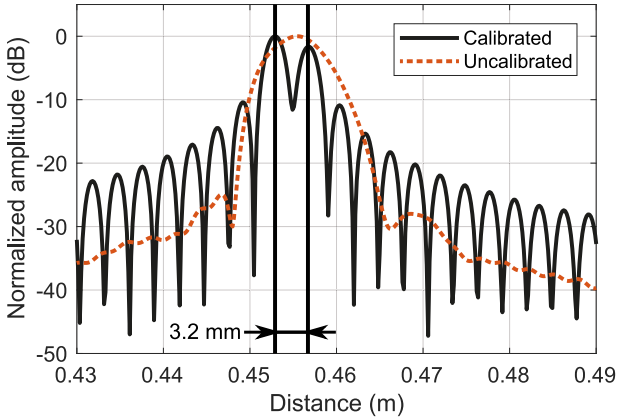

Fig. 15. Measured spectrum of two targets separated 3.2 mm in range direction with and without IF amplitude calibration.

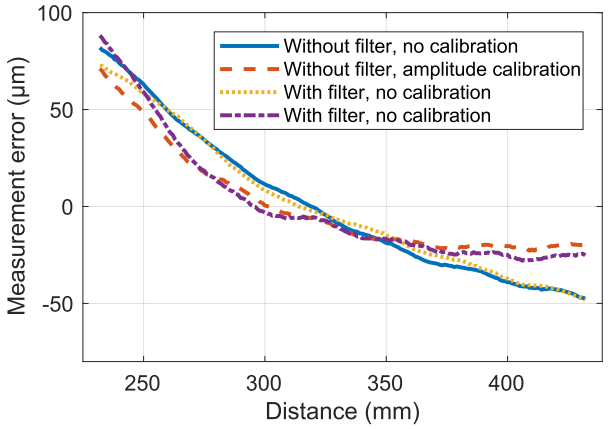

Fig. 16. Distance error without any distance correction in a range from 230 to 430 mm with a step width of 200 μm.

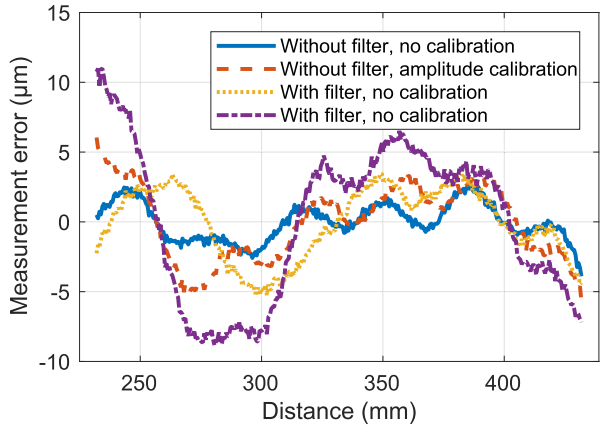

Fig. 17. Distance error in a range from 230 to 430 mm. For calibration, a static quadratic correction was used.

calibration factor, a simple metal plate at a different distance was used. It can be seen that in the uncalibrated case, only one target peak is discernible, even though the bandwidth of 52 GHz should allow a separation of both targets. The calibrated measurement, on the other hand, allows a clear separation of both targets, showing the successful calibration. This makes the full range resolution usable.

C. Distance Accuracy

For distance accuracy measurements, a flat metal reflector was mounted on a high-precision linear stage. The whole setup is already shown in Fig. 11. An Attocube FPS1010 laser interferometer providing a range accuracy in the nanometer regime was used as a reference system within the distance accuracy measurement setup. It was used on the same axis as the radar using the backside of the movable target in Fig. 11. The measurement distance was varied from 230 to 430 mm with a step width of 200 μm. Each measurement was repeated four times, with and without the dielectric filter described in Section IV-A and with and without the amplitude calibration described in Section IV-B. A down ramp ranging from 250–198 GHz with a ramp time of 15 ms was used as the frequency chirp.

In Fig. 16, the measured distance error out of the box without any particular distance correction is shown. In summary, the measurement error lays between -50 and $+100$ μm and shows a parabolic slope over the distance. Using the dielectric filter described above increases the distance error by 17 μm mainly preserving the parabolic slope, while the amplitude calibration described in Section IV-B is affecting the parabolic slope. For all combinations of filter usage and amplitude calibration, it could be proved by several measurements that the parabolic slope was stable and constant for each configuration, indicating a systematic error of the system and measurement setup, whereby the parabolic error can be calibrated.

For removing the parabolic error, reference measurements were taken and a best-fit paraboloid was calculated, which is used as fixed compensation data. With these compensation data, the measurement was repeated and corrected. The resulting distance measurement error is shown in Fig. 17. The lowest error with $d_{\text{error}} = -3.9$ to $+2.8$ μm is achieved without filter and without amplitude correction. The use of the filter and amplitude correction increases the measurement error to $d_{\text{error}} = -9.1$ to $+11.3$ μm, which is still an outstanding result for radar measurements over a measurement distance of multiple wavelengths.

When examining the remaining error, it can be observed that for smaller intervals in range direction, the error is locally much more constant; therefore, a much better correction of systematic errors can be achieved. Based on the distance error plotted in Fig. 16, the measurement error in the range of $d = 270$ mm $- 280$ mm can be reduced to $d_{\text{error}} = \pm 5$ μm just by considering a constant offset without any further correction. As the measurement error in this range shows a linear systematic error, a linear best-fit line can be used as compensation data, leading to the distance measurement error shown in Fig. 18. The measured distance error in short distance intervals can be reduced down to $d_{\text{error}} = -0.5$ to $+0.4$ μm just by a linear correction, which is an outstanding result.

The slightly increased measurement error when the dielectric filter is used is caused by the additional loss the filter causes in the signal path. This additional loss reduces the SNR, increasing the noise-like distance error. The slightly increased

TABLE I
COMPARISON OF RADAR SENSORS WITH AN OPERATING FREQUENCY ABOVE 100 GHz

Reference	Center frequency (GHz)	Bandwidth (GHz)	Relative Bandwidth	Peak Power (dBm)	Phase noise (dBc/Hz @ 10 kHz)	Synthesizer	Technology	Assembly
[19]	240	60	25.0%	3 (EIRP)		PLL/DDS	SiGe	MMIC + ext. RF signal
[21]	300	27	9.0%	-1		DDS	unspecified	Split-block
[23]	156	16	10.3%	5	-76	PLL	SiGe	MMIC + ext. RF signal
[20]	146	48	32.9%	-1	-84	PLL	SiGe	Fully integrated MMIC
[22]	220	40	18.2%	5		DDS	GaAs	Split-block
[5],[8]	215	30	14.0%	5		DDS	unspecified	MMIC + ext. RF signal
[24]	122.5	1	0.8%	-4		PLL	SiGe	Fully integrated MMIC
[18][i]	140	20	14.5%	-2	-96.5 (@ 1 MHz)	VCO only	CMOS	
This work	224	52	23.2%	1.8	-75.6	PLL	SiGe	Fully integrated MMIC

[i] VCO only, for comparison.

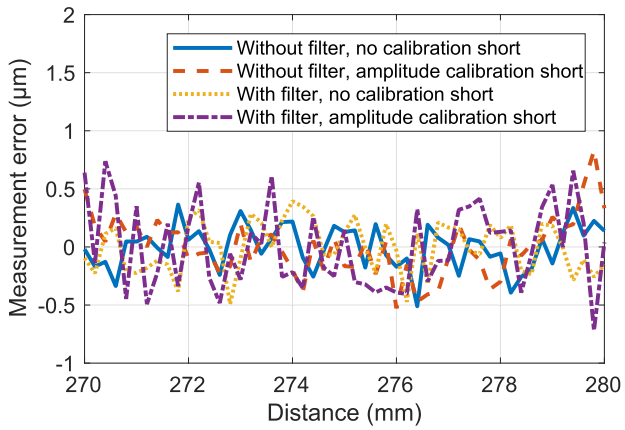

Fig. 18. Distance error in a reduced distance interval from 270–280 mm. To calibrate the systematic error, a static linear correction was used.

measurement error with the use of the amplitude calibration is caused by another effect. As shown in Fig. 14, the IF signal amplitude gets very small at the end of the ramp, causing a very large calibration factor. Due to the large magnitude of the calibration factor, also the noise which is included in the IF signal is amplified, leading to an increased measurement error.

These measurements show that this radar system is well suited for high-precision distance measurements in a wide range of industrial applications or high-resolution imaging tasks. The filter for removing false targets and the amplitude calibration for improving the range resolution slightly increase the distance measurement error. Therefore the use of the filter or the amplitude calibration is a tradeoff between accuracy, unambiguousness, and range resolution which has to be made for the intended application the sensor is designated for.

V. COMPARISON

In Table I, an overview of radar systems with an operating frequency above 100 GHz is given. For radar sensors above 100 GHz, the D-band (110–170 GHz) and the WR3 waveguide band (220–330 GHz) are the most relevant, as both frequency bands contain a license free ISM band at 122 and 244 GHz, respectively. Most of these systems are using SiGe or III–V technologies such as GaAs. A complete radar system working above 100 GHz based on CMOS devices was not found to the best of the authors knowledge. For comparison, a stand-alone VCO presented in [18] is given in Table I. For frequency synthesis, either PLL or DDS-based system architectures can be found, as well as a combination of both. As the bandwidth is determining the range resolution, this is an important feature for high-resolution and high-accuracy measurements. There are only few complete radar transceivers above 100 GHz, achieving a relative modulation bandwidth larger than 20% ([19], [20], and this paper). In terms of the scale of integration, all transceivers can be divided into three groups. Some of the sensors are realized with split-block components [21], [22], mostly used by III–V semiconductors, allowing a low loss connection between separate components but leading to bulky dimensions of the sensor. The next stage of integration is to merge most of the RF components into a single MMIC containing the transmitter path, including frequency multipliers or up-converting mixers in combination with the receiver circuitry [5], [8], [19], [23]. This allows much more compact transceivers, which still need external signal sources for generating the RF signals. The highest grade of integration is achieved by fully integrated MMICs containing all RF parts, including signal sources and TX/RX paths ([20], [24], and this paper). With the use of fully integrated transceiver MMICs, no external RF circuitry is needed, enabling compact and robust realizations for stand-alone operation. In terms of the output power, peak values ranging from -4 to 5 dBm can be found. Due to usually larger breakdown voltages, III–V technologies are known for larger output powers compared to SiGe technologies, but with [23], a SiGe-based radar sensor with 5-dBm output power is presented catching up to realizations based on GaAs like [22], also providing an output power of 5 dBm. In terms of output power, the presented sensor is positioned midfield with an peak output power of 1.8 dBm, which is sufficient for measurement distances up to several meters, as the sensors' intended uses are short range

industrial applications. Focusing on high-precision measurements, the distance accuracy is one of the most interesting and, at the same time, most difficult points for comparison. There are only a few radar sensors presented, including distance accuracy measurements. Additionally, the measurement setup as well as the signal processing has a huge influence of the results. In [24], distance measurements using a commercially available radar transceiver are presented, featuring a distance accuracy of -200 to $+150$ μm over a range of 1800 mm and ± 2 μm over a range of 5 mm, focusing on the use of a special phase evaluation algorithm. Reference [25] shows distance measurements for the use in micro machining using an 80-GHz sensor, reaching a distance accuracy of 0.5 μm using a phase evaluation algorithm, while the measurements are limited to a range of 2 mm. In [26], measurements with a similar 80-GHz sensor are presented, showing a distance accuracy of -4 to $+3$ μm over a range of 50 mm. In the frequency range above 100 GHz, [20] presents a D-band radar sensor, reaching a distance accuracy of -0.5 to $+1$ μm over a range of 10 mm. Compared to these measurements, the presented sensor offers an outstanding distance accuracy down to $d_{\text{error,200 mm}} = -3.9$ to $+2.8$ μm over a range of 200 mm and $d_{\text{error,10 mm}} = -0.5$ to $+0.4$ μm over a reduced range of 10 mm, making this sensor feasible for a wide range of industrial high-precision measurement tasks.

VI. Conclusion

In this paper, an ultra compact radar sensor is presented. It is aimed for the use in industrial, security, and automotive applications, providing a cost effective, compact, and robust alternative to conventional sensor solutions. With a tuning range of 52 GHz around a center frequency of 224 GHz, high-resolution and high-accuracy measurements are possible even under harsh environmental conditions. The compact and high-focusing antenna setup allows well-defined measurement spots even under constricted space requirements. Through the correction of systematic errors, an accuracy of the measurement system down to -3.9 to $+2.8$ μm is shown, making this radar sensor suitable for multiple applications where radar sensors were not usable before. For applications where only a short range interval is relevant, for example in displacement measurements, an measurement error of $d_{\text{error}} = -0.5$ to $+0.4$ μm after a linear compensation is achieved, which is an outstanding result. Additionally, filter and calibration methods are presented to optimize the range unambiguousness and increase the range resolution close to the theoretical limit. Combining these details and advantages of the presented sensor, a modern measurement solution is presented to fulfill the needs of various present and future measurement and imaging tasks.

Acknowledgment

The authors would like to thank Infineon Technologies AG and its staff for fabricating the MMIC chips.

References

[1] X. Chen, F. Liu, Q. Hou, and Y. Lu, "Industrial high-temperature radar and imaging technology in blast furnace burden distribution monitoring process," in *Proc. 9th Int. Conf. Electron. Meas. Instrum.*, Aug. 2009, pp. 1-599–1-603.

[2] M. Vogt and M. Gerding, "Silo and tank vision: Applications, challenges, and technical solutions for radar measurement of liquids and bulk solids in tanks and silos," *IEEE Microw. Mag.*, vol. 18, no. 6, pp. 38–51, Sep./Oct. 2017.

[3] D. Brumbi, "Measuring process and storage tank level with radar technology," in *Proc. Int. Radar Conf.*, May 1995, pp. 256–260.

[4] D. Nuessler, N. Pohl, J. Kuels, K. Hein, and D. Stein, "THz imaging for recycling of black plastics," in *Proc. German Microw. Conf. (GeMiC)*, Mar. 2014, pp. 1–4.

[5] D. A. Robertson, D. G. Macfarlane, and T. Bryllert, "A 220 GHz 3D imaging radar with sub-cm^3 voxel resolution for security applications," in *Proc. Eur. Radar Conf. (EuRAD)*, Oct. 2016, pp. 398–401.

[6] T. Jaeschke, C. Bredendiek, and N. Pohl, "3D FMCW SAR imaging based on a 240 GHz SiGe transceiver chip with integrated antennas," in *Proc. German Microw. Conf.*, Mar. 2014, pp. 1–4.

[7] J. Barowski, M. Zimmermanns, and I. Rolfes, "Millimeter-wave characterization of dielectric materials using calibrated FMCW transceivers," *IEEE Trans. Microw. Theory Techn.*, vol. 66, no. 8, pp. 3683–3689, Aug. 2018.

[8] D. G. Macfarlane, D. A. Robertson, and T. Bryllert, "Pathfinder—A high resolution 220 GHz imaging radar providing phenomenological data for security scanner development," in *Proc. 41st Int. Conf. Infr., Millim., THz. Waves (IRMMW-THz)*, Sep. 2016, pp. 1–2.

[9] A. Shoykhetbrod, T. Geibig, A. Hommes, R. Herschel, and N. Pohl, "Concept for a fast tracking 60 GHz 3D-radar using frequency scanning antennas," in *Proc. Int. Conf. Infr., Millim., THz. Waves (IRMMW-THz)*, Sep. 2016, pp. 1–3.

[10] M. Schroter *et al.*, "The EU DOTSEVEN project: Overview and results," in *Proc. IEEE Compound Semiconductor Integr. Circuit Symp. (CSICS)*, Oct. 2016, pp. 1–4.

[11] S. Thomas, C. Bredendiek, T. Jaeschke, F. Vogelsang, and N. Pohl, "A compact, energy-efficient 240 GHZ FMCW radar sensor with high modulation bandwidth," in *Proc. German Microw. Conf. (GeMiC)*, Mar. 2016, pp. 397–400.

[12] J. Böck *et al.*, "SiGe HBT and BiCMOS process integration optimization within the dotseven project," in *Proc. IEEE Bipolar/BiCMOS Circuits Technol. Meeting (BCTM)*, Oct. 2015, pp. 121–124.

[13] C. Bredendiek, N. Pohl, T. Jaeschke, K. Aufinger, and A. Bilgic, "A 240 GHz single-chip radar transceiver in a SiGe bipolar technology with on-chip antennas and ultra-wide tuning rang," in *Proc. IEEE Radio Freq. Integr. Circuits Symp. (RFIC)*, Jun. 2013, pp. 309–312.

[14] N. Pohl, T. Jaeschke, and K. Aufinger, "An ultra-wideband 80 GHz FMCW radar system using a SiGe bipolar transceiver chip stabilized by a fractional-N PLL synthesizer," *IEEE Trans. Microw. Theory Techn.*, vol. 60, no. 3, pp. 757–765, Mar. 2012.

[15] N. Pohl and M. Gerding, "A dielectric lens-based antenna concept for high-precision industrial radar measurements at 24GHz," in *Proc. Eur. Microw. Conf. (EuMC)*, Oct. 2012, pp. 731–734.

[16] K. Harima, "Accurate gain measurement for millimeter-wave horn and open-ended waveguide antennas," in *Proc. Int. Symp. Antennas Propag. (ISAP)*, Oct./Nov. 2012, pp. 1019–1022.

[17] T. Jaeschke, C. Bredendiek, and N. Pohl, "A 240 GHz ultra-wideband FMCW radar system with on-chip antennas for high resolution radar imaging," in *IEEE MTT-S Int. Microw. Symp. Dig.*, Jun. 2013, pp. 1–4.

[18] Y.-T. Chang and H.-C. Lu, "A D-band wide tuning range VCO using switching transformer," in *IEEE MTT-S Int. Microw. Symp. Dig.*, Jun. 2017, pp. 1353–1355.

[19] K. Statnikov, N. Sarmah, J. Grzyb, S. Malz, B. Heinemann, and U. R. Pfeiffer, "A 240 GHz circular polarized FMCW radar based on a SiGe transceiver with a lens-integrated on-chip antenna," in *Proc. Eur. Radar Conf. (EuRad)*, Oct. 2014, pp. 447–450.

[20] T. Jaeschke, C. Bredendiek, S. Kuppers, and N. Pohl, "High-precision D-band FMCW-radar sensor based on a wideband SiGe-transceiver MMIC," *IEEE Trans. Microw. Theory Techn.*, vol. 62, no. 12, pp. 3582–3597, Dec. 2014.

[21] J. Grajal *et al.*, "3-D high-resolution imaging radar at 300 GHz with enhanced FoV," *IEEE Trans. Microw. Theory Techn.*, vol. 63, no. 3, pp. 1097–1107, Mar. 2015.

[22] T. Bryllert, V. Drakinskiy, K. B. Cooper, and J. Stake, "Integrated 200–240-GHz FMCW radar transceiver module," *IEEE Trans. Microw. Theory Techn.*, vol. 61, no. 10, pp. 3808–3815, Oct. 2013.

[23] M. Hitzler, P. Grüner, L. Boehm, W. Mayer, and C. Waldschmidt, "On monostatic and bistatic system concepts for mm-wave radar MMICs," *IEEE Trans. Microw. Theory Techn.*, vol. 66, no. 9, pp. 4204–4215, Sep. 2018.
[24] S. Scherr *et al.*, "Miniaturized 122 GHz ISM band FMCW radar with micrometer accurac," in *Proc. Eur. Radar Conf. (EuRAD)*, Sep. 2015, pp. 277–280.
[25] S. Ayhan *et al.*, "Millimeter-wave radar distance measurements in micro machining," in *Proc. IEEE Topical Conf. Wireless Sensors Sensor Netw. (WiSNet)*, Jan. 2015, pp. 65–68.
[26] N. Pohl *et al.*, "Radar measurements with micrometer accuracy and nanometer stability using an ultra-wideband 80 GHz radar system," in *Proc. IEEE Topical Conf. Wireless Sensors Sensor Netw. (WiSNet)*, Jan. 2013, pp. 31–33.

Sven Thomas (M'09) was born in Bochum, Germany, in 1987. He received the M.Sc. degree in electrical engineering from Ruhr University Bochum, Bochum, Germany, in 2013.

Since 2013, he has been a Research Assistant with the Department of Integrated Circuits and Sensor Systems, Fraunhofer Institute for High Frequency Physics and Radar Techniques, Wachtberg, Germany. His current research interests include the design of integrated SiGe circuits and the development of system concepts for industrial radar-based measurement systems with operating frequencies up to 300 GHz.

Mr. Thomas was a recipient of the Argus Award of Cassidian in 2012 and was a co-recipient of the EuMIC Best Paper Award from the European Microwave Week in 2012 and the 2015 Best Demo Award of IEEE Radio Wireless Week.

Christian Bredendiek (M'12) was born in Gelsenkirchen, Germany, in 1981. He received the Dipl.Ing. and Dr.Ing. degrees in electrical engineering from Ruhr University Bochum, Bochum, Germany, in 2008 and 2014, respectively.

From 2008 to 2014, he was a Research Assistant with the Institute of Integrated Systems, Ruhr University Bochum. Since 2015, he has been with the Department of Integrated Circuits and Sensor Systems, Fraunhofer Institute for High Frequency Physics and Radar Techniques, Wachtberg, Germany. His current research interests include frequency synthesis, working on system concepts and integrated circuits for various mm-wave applications.

Dr. Bredendiek was a recipient of the EuMIC Best Paper Award from European Microwave Week in 2012.

Nils Pohl (S'07–M'11–SM'14) received the Dipl.-Ing. and Dr.Ing. degrees in electrical engineering from Ruhr University Bochum, Bochum, Germany, in 2005 and 2010, respectively.

From 2006 to 2011, he was a Research Assistant with the Institute of Integrated Systems, Ruhr University Bochum, where he was involved in integrated circuits for millimeter-wave (mm-wave) radar applications. In 2011, he became an Assistant Professor with Ruhr University Bochum. In 2013, he became the Head of the Department of Millimeter-Wave Radar and High Frequency Sensors, Fraunhofer Institute for High Frequency Physics and Radar Techniques, Wachtberg, Germany. In 2016, he became a Full Professor of integrated systems with Ruhr University Bochum. He has authored or coauthored more than 100 scientific papers and holds several patents. His current research interests include ultra-wideband mm-wave radar, design, and optimization of mm-wave integrated SiGe circuits and system concepts with frequencies up to 240 GHz and above, as well as frequency synthesis and antennas.

Dr. Pohl is a member of the VDE, ITG, EUMA, and URSI. He was a co-recipient of the 2009 EEEfCom Innovation Award, the 2012 EuMIC Prize, the 2015 Best Demo Award of IEEE Radio Wireless Week, and the 2016 ICECS Best Paper Award. He was a recipient of the Karl-Arnold Award of the North Rhine-Westphalian Academy of Sciences, Humanities and the Arts in 2013 and the IEEE MTT-S Outstanding Young Engineer Award in 2018.